

SPECIAL ISSUE ARTICLE

Insight of $\text{BaCe}_{0.5}\text{Fe}_{0.5}\text{O}_{3-\delta}$ twin perovskite oxide composite for solid oxide electrochemical cells

Zeyu Zhao  | Minda Zou | Hua Huang | Ximei Zhai | Harrison Wofford  | Jianhua Tong Materials Science and Engineering,
Clemson University, Clemson, South
Carolina, USA**Correspondence**Jianhua Tong, Materials Science and
Engineering, Clemson University,
Clemson, SC 29634, USA.
Email: jianhut@clemson.edu**Funding information**US Department of Energy's Office of
Energy Efficiency and Renewable Energy
(EERE) under the Fuel Cell Technologies
Office, Grant/Award Number:
DE-EE0008428; National Aeronautics and
Space Administration (NASA),
Grant/Award Number: #80NSSC20M0233**Abstract**

One-pot synthesized twin perovskite oxide composite of $\text{BaCe}_{0.5}\text{Fe}_{0.5}\text{O}_{3-\delta}$ (BCF), comprising cubic and orthorhombic perovskite phases, shows triple-conducting properties for promising solid oxide electrochemical cells. Phase composition evolution of BCF under various conditions was systematically investigated, revealing that the cubic perovskite phase could be fully/partially reduced into the orthorhombic phase under certain conditions. The reduction happened between the two phases at the interface, leading to the microstructure change. As a result, the corresponding apparent conducting properties also changed due to the difference between predominant conduction properties for each phase. Based on the revealed phase composition, microstructure, and electrochemical properties changes, a deep understanding of BCF's application in different conditions (oxidizing atmospheres, reducing/oxidizing gradients, cathodic conditions, and anodic conditions) was achieved. Triple-conducting property ($\text{H}^+/\text{O}^{2-}/\text{e}^-$), fast open-circuit voltage response ($\sim 16\text{--}470$ mV) for gradients change, and improved single-cell performance ($\sim 31\%$ lower polarization resistance at 600°C) were comprehensively demonstrated. Besides, the performance was analyzed under anodic conditions, which showed that the microstructure and phase change significantly affected the anodic behavior.

KEYWORDS

electrochemistry, energy conversion, fuel cells, nanocomposites, perovskites

1 | INTRODUCTION

Perovskite oxides with unique electrical properties, such as ionic (oxygen ionic or protonic), electronic, or mixed ionic and electronic conductivities, have found extensive applications (solid oxide cells, membrane reactors, chemical sensors, and oxidation and thermochemical fuel production catalysts) for energy conversion, storage, and harvesting.^{1–6} In recent years, some perovskite oxides (e.g.,

triple conducting oxides and co-ionic conducting oxides) allowing the simultaneous transport of oxygen ions and protons have attracted significant attention because of their outstanding performance as oxygen electrodes^{7–9} and co-ionic electrolytes^{10,11} for solid oxide cells (e.g., solid oxide fuel/electrolysis cells [SOFC/ECs] and protonic ceramic fuel cell/ECs [PCFC]). The strategy of adjusting dopants and structural symmetries has been intensively investigated for discovering new multiple ionic conducting

This is an open access article under the terms of the [Creative Commons Attribution-NonCommercial](https://creativecommons.org/licenses/by-nc/4.0/) License, which permits use, distribution and reproduction in any medium, provided the original work is properly cited and is not used for commercial purposes.

© 2022 The Authors. *Journal of the American Ceramic Society* published by Wiley Periodicals LLC on behalf of American Ceramic Society.

(MIC) phase-pure perovskite oxides.^{7,9,12} However, both proton and oxygen ion conductivity originated from the oxygen vacancy introduced by the accepted dopant in the B-site of the ABO_3 perovskite structure, which was significantly constrained by the limited dopant solubility and operating conditions (e.g., temperatures and atmospheres).^{13–15}

The integration of proton-conducting perovskite oxides and oxygen ion-conducting perovskite oxides to form MIC composites provides a more facile way to combine proton and oxygen ion conductivities. The easiness and independence of adjusting the different phases' fractions allow more freedom to engineer the composites' partial conductivities. The mechanical mixing^{8,16} and infiltration^{12,17} are the most straightforward methods to prepare MIC composites, which, however, frequently results in poor two-phase percolation microstructures, slow solid-state interfacial reactions, precipitation of new phases, and rapid performance degradations.^{18,19} The high-performance and stable MIC composites consisting of two perovskite phases of different symmetries (e.g., orthorhombic and cubic perovskites) have been synthesized using the facile one-pot synthesis method and utilized as oxygen electrodes for solid oxide cells.^{20–22} Because of the simultaneous formation and the similar crystal structures of the two componential perovskite phases, this new type of composites was called twin-perovskite oxide composites (TPOCs) in our previous work.²³ The TPOCs usually have better microstructure and stability than composites fabricated by mechanical mixing and infiltration methods because the high-temperature calcination of the well-dispersed componential precursor mixture could easily reach thermodynamic equilibrium. However, except for the performance, most of the other information, specifically the phase and microstructure evolution and stability versus experimental conditions, which determine the potential applications, are needed desperately to explore the applications of this new family of MIC materials.

The TPOC with a nominal composition of $BaCe_{0.5}Fe_{0.5}O_{3-\delta}$ (BCF) comprised a Ce-rich orthorhombic phase, and an Fe-rich cubic phase was first discovered as a promising triple conducting cathode for PCFCs, which showed much better performance compared with phase-pure parent perovskite oxides.²¹ After that, it was also demonstrated as a promising cathode for SOFCs and an excellent hydrogen permeation membrane.^{24,25} In these reports, the authors claimed that the Ce-rich orthorhombic phase was responsible for proton conduction, whereas the Fe-rich cubic phase was for mixed oxygen ion and electron conduction. The driving force for the formation of TPOC during the one-pot synthesis was suggested to be the significant radii change of multivalent elements and resulting lattice stress of mismatch between two-phase structures.^{25–27} It could be imagined

that applied atmospheres at certain temperatures may significantly affect the phase compositions and achieve different conduction properties for various application circumstances in solid oxide electrochemical cells, which have not been investigated in previous reports. Therefore, it is necessary to carefully investigate the atmosphere dependence of phase compositions, microstructures, and electrochemical properties for BCF to explore the potential of BCF working as component materials of solid oxide electrochemical cells.

Herein, we applied various atmospheres and temperatures to determine the change of BCF samples in aspects of phase compositions, microstructures, and electrochemical properties. Based on these results, demonstrations of BCF in several electrochemical application conditions were conducted to evaluate its feasibility, which provided the guidance for further research of BCF and showed an exemplar analysis methodology for other TPOCs.

2 | EXPERIMENTAL PROCEDURES

2.1 | Preparation of BCF powders

BCF powders were synthesized by a modified Pechini method through one-pot synthesis to achieve thermodynamic equilibrium during synthesis, which was reported in our previous work.²³ Figure 1 describes the detailed synthesis procedures for four types of BCF powders studied in this work. Stoichiometric amounts of $Ba(NO_3)_2$ (99+%, Alfa Aesar), $Ce(NO_3)_3 \cdot 6H_2O$ (99.5 wt%, Alfa Aesar), and $Fe(NO_3)_3 \cdot 9H_2O$ (98+%, Alfa Aesar) salts were first added to the appropriate amount of deionized water in a Pyrex glass beaker. The ethylenediaminetetraacetic (99.4%, Alfa Aesar) acid and citric acid monohydrate (99.5%, Acros Organics) powders with molar ratios of 1.5 and 1 to total metal ions were added to the mixture during magnetic stirring. After slowly adding ammonium hydroxide ($NH_3 \cdot H_2O$, 28%–30% w/w, LabChem) to adjust pH around 10, all the solids dissolved and formed a clear solution. The clear solution became a homogeneous and viscous gel after gradually vaporizing the extra water at around 80–90°C. The gel turned into dark charcoal-like primary powder after being dried at 150°C for 48 h in a box oven. Then the powder was fired at 600°C for 5 h to get rid of most of the carbon. After being ball-milled for 7 days in the 1-butanol (Alfa Aesar) solvent with yttria-stabilized zirconia (YSZ) balls as grinding media, the particle size of the primary powder was further brought down. After evaporating at 90°C and firing at 500°C, the powder was further dispersed in isopropanol by ball-milling for another 3 days to remove agglomeration that might form during the firing process. The fine BCF precursor powder was collected after further drying at 90°C for 48 h. The followed final calcination at

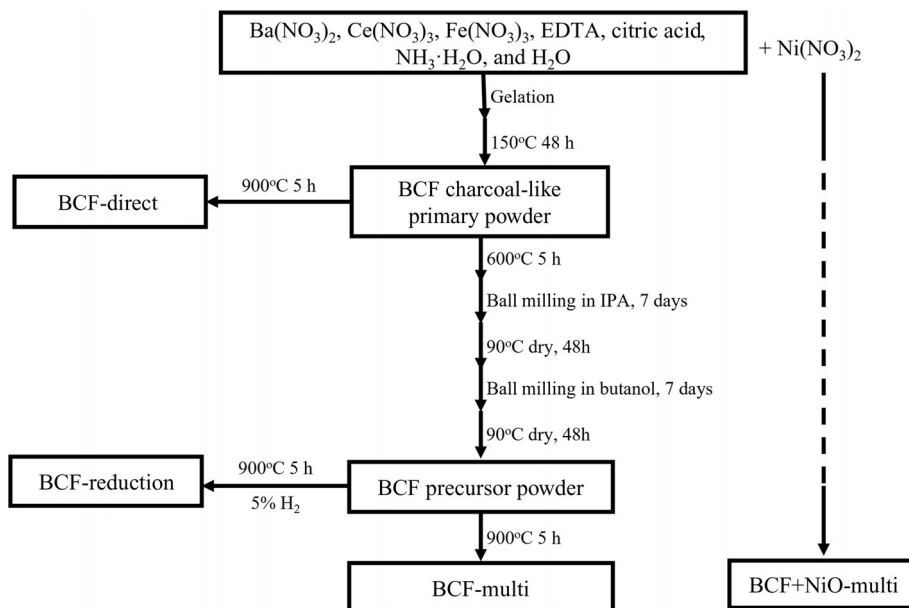


FIGURE 1 The flowchart of BCF powder synthesis under different conditions

900°C for 5 h under stagnant air achieved the crystallized BCF composite powder, denoted as BCF-Multi.

Also, the BCF powders were synthesized by directly firing the charcoal-like primary or precursor powders through different post-processing. The direct calcination of charcoal-like primary powder at 900°C 5 h in the box furnace under stagnant resulted in BCF-Direct powder. The firing of the precursor powder under flowing dry 5 vol% H₂ (balanced by Ar) in a tubular furnace using the same time and temperature resulted in BCF-Reduction powder. Besides, the BCF + 20-mol% NiO powder (BCF + NiO-Multi) was synthesized by following the same procedure as that for BCF-Multi powder with additional Ni(NO₃)₂ (98%, Alfa Aesar) added together with other chemicals at the first step.

To further study the structure evolution of BCF composite powder, some specifically designed reduction and reoxidation experiments were performed. A proper amount of the as-prepared BCF-Direct powder was placed in an alumina boat and treated in a tubular furnace at elevated temperatures with a flow rate of 50 ml min⁻¹ in a 5% H₂ atmosphere for reduction treatment. With a 5°C/min ramping rate, the furnace was heated up to 900°C and held for 24 h. After cooling to the room temperature at the same rate, the reoxidation was conducted by heating reduced BCF powder to 900°C in the flowing air, and all other conditions were kept the same. The same reduction-reoxidation experiments for the BCF-Direct powders were performed at 600 and 750°C.

For the reduction treatments to simulate the phase evolution during the investigation of anode application, the BCF-Direct powder was treated under dry 5% H₂ with a flow rate of 50 ml min⁻¹. After the 24-h treatment, the

gas was switched into dry H₂ with the same flowing rate for another 24-h treatment. Then, the atmospheres were changed into wet 5% H₂ (humidified by flow through the bubbler at room temperature) and wet H₂ for 24-h each, sequentially.

2.2 | Preparation of electrolyte and anode precursor powders

The BaZr_{0.8}Y_{0.2}O_{3-δ} (BZY20) + 1 wt% NiO and BaCe_{0.7}Zr_{0.1}Y_{0.1}Yb_{0.1}O_{3-δ} (BCZYYb) + 1 wt% NiO electrolyte precursor powders, and BCZYYb-NiO anode precursor powder were prepared by mechanically mixing raw material powders. Taking BCZYYb precursor as an example, proper amounts of BaCO₃ (Alfa Aesar, 99.8%), CeO₂ (Alfa Aesar, 99.9%), ZrO₂ (Alfa Aesar, 99.7%), Y₂O₃ (Alfa Aesar, 99.9%), and Yb₂O₃ (Alfa Aesar, 99.9%) were mixed in the stoichiometry ratio of BCZYYb. A sintering aid of 1 wt% NiO was added to the precursor mixture and ball-milled for 48 h with 3-mm YSZ balls grinding media and isopropanol as the grinding solvent. The slurry was then heated at 150°C in a box oven for 48 h to dry thoroughly. The BCZYYb anode precursor containing ~60 wt% NiO + 20 wt% (based on total solid) starch was prepared using the same procedure.

2.3 | Preparation of electrode/electrolyte pastes

The fine BCF precursor powder with a much smaller particle size was used to prepare the electrode precursor paste

to prepare BCF electrodes with desired porous nanostructures. The BCF precursor powder, dispersant solution (20 wt% Solsperse 28000 [Lubrizol] in terpineol solution), and binder solution (5 wt% V-600 [Heraeus] in terpineol solution) with a weight ratio of 15:3:1 were manually mixed in an agate mortar using an agate pestle for 45 min, resulting in BCF cathode paste. Following the same procedure, the BCF + 20-mol% NiO anode paste and the BCZYYb electrolyte paste were prepared from their precursor powders, respectively.

2.4 | Preparation of electrolyte pellets

The BCF pellets were made using the conventional ceramic processing method of dry-pressing and furnace-sintering. To be formed into green pellets, BCF-Direct powder was first dry-pressed for 120 s under ~ 400 MPa in circular carbon-aided steel die set with a diameter of 19 mm. The green pellets with a thickness of ~ 1 mm were then sintered for 12 h at 1300°C to achieve the final sintered BCF pellets. The BCZYYb + 1 wt% NiO and BZY20 + 1 wt% NiO electrolyte pellets were prepared using the same procedures. The precursor powder of BCZYYb + 1 wt% NiO or BZY20 + 1 wt% NiO electrolyte was pressed into green pellets under 350 MPa for 120 s with a diameter of 19 mm and a thickness of ~ 2 mm. The BCZYYb/BZY20 electrolyte pellets were obtained after sintering at 1450°C for 18 h.

2.5 | Preparation of symmetric cells

The electrode/electrolyte/electrode configuration was used to prepare symmetrical cells. The BCF or BCF + 20-mol% NiO precursor paste was screen printed on both sides of the polished electrolyte pellets before being annealed at 900°C for 5 h. The silver paste was applied to both sides of the sample using a screen-printing method before electrochemical measurements. Then, to act as current collectors and lead wires (four probes), silver mesh (Alfa Aesar, item number 40936) and gold wire (Alfa Aesar, item number 00725) were attached to the silver paste surfaces (Alfa Aesar, item number 44075). Finally, the sample was dried at 150°C on a hot plate to ensure good adhesion.

2.6 | Fabrication of single cells

The single-cell based on BCZYYb half-cell with BCF cathode was fabricated. The anode green pellets were produced by dry pressing of BCZYYb anode precursor powder at 350 MPa for 120 s in circular carbon-aided steel die set, with

a diameter of 19 mm and a thickness of 2 mm. Electrolyte layers were screen-printed on both sides of green anode pellets using electrolyte paste and then fired at 1450°C for 18 h. The extra electrolyte layer was removed from sintered pellets, and the electrolyte layer was screen-printed with BCF paste ($\sim 20\ \mu\text{m}$) of 12 mm in diameter. After that, the entire structure was fired at 900°C for 5 h. Silver mesh and gold wire were used as current collectors before the single-cell tests, and they were attached to the electrode surfaces with silver paste.

2.7 | Characterization

The X-ray diffraction (XRD) patterns were recorded using a Rigaku Ultima IV diffractometer with monochromatic Cu K radiation ($1.5406\ \text{\AA}$) with as-prepared powder samples or crushed down powders from dense pellets. The scanning rate was $1^\circ/\text{min}$ with a 0.02° step length and a 20° – 80° 2θ scan range. Scanning electron microscopy (SEM) of BCF powders and pellets was studied using a Hitachi S-4800 microscope with a 10-kV acceleration voltage and a $10\text{-}\mu\text{A}$ emission current. Moreover, the backscattering SEM was also conducted at the Hitachi S-4800 with the YAG-BSE (yttrium aluminum garnet-backscatter electron) detector under a similar condition.

Symmetrical cells were measured by Gamry Reference 600 Plus Potentiostat electrochemical impedance spectra (EIS) over a range of temperatures 300 – 700°C under wet flowing air (through room-temperature water bubbler, $50\ \text{ml min}^{-1}$) using a signal amplitude of 10 mV in the frequency range of 0.01 Hz–5 MHz. The temperature increased to 700°C with a $2^\circ\text{C}/\text{min}$ ramping rate, and the sample was held to stabilize for 1 h at this temperature, and subsequent temperature points down to 300°C with a 50°C step size. Results obtained from EIS were further analyzed with ZView software. The BCF + 20 mol% NiO symmetrical cells were measured under the sequenced atmospheres of dry 5% H_2 , dry H_2 , wet 5% H_2 , and wet H_2 with $50\ \text{ml min}^{-1}$ for 24 h for each at 750°C .

The performance of the fuel cell was taken by a Gamry Reference 3000 from 550 to 700°C . The flowing air was applied on the cathode side, and the anode side was reduced by 5% H_2 and pure H_2 for 24 h, separately. Following that, EIS (with a perturbation voltage of 10 mV and a frequency range of 0.01 Hz–1 MHz), cyclic voltammetry, Potentiostat EIS, and open-circuit voltages (OCVs) were used.

The concentration cell's electromotive force (EMF) test was obtained by applying each side under different atmospheres with controlled gas compositions to determine the transfer numbers from 400 to 700°C . The testing concentration cells with the following construction²⁸:

Gas(I), Ag electrode(I)/BCF dense pellet/Ag electrode(II), gas(II).

BCF conducts protons, oxygen ions, and electron holes in our case. Theoretical EMFs (V_{cal}) could be expressed by the following equation, in which R is the ideal gas constant, F is the Faraday constant, T is the temperature, t is the transfer number (marked with species), and the p is the partial pressure of gas species at different electrodes marked with superscripts of I and II:

$$V_{\text{cal}} = t_{\text{H}^+} \frac{RT}{2F} \ln \left(\frac{p_{\text{H}_2}^{\text{I}}}{p_{\text{H}_2}^{\text{II}}} \right) + t_{\text{O}_2^-} \frac{RT}{4F} \ln \left(\frac{p_{\text{O}_2}^{\text{II}}}{p_{\text{O}_2}^{\text{I}}} \right) \quad (1)$$

As we take the water formation (Equation 2) into account, Equation (1) could be rewritten as Equation (3) under oxidation atmospheres:



$$V_{\text{cal}} = (t_{\text{H}^+} + t_{\text{O}_2^-}) \frac{RT}{4F} \ln \left(\frac{p_{\text{O}_2}^{\text{II}}}{p_{\text{O}_2}^{\text{I}}} \right) + t_{\text{H}^+} \frac{RT}{2F} \ln \left(\frac{p_{\text{H}_2\text{O}}^{\text{I}}}{p_{\text{H}_2\text{O}}^{\text{II}}} \right) \quad (3)$$

The EMF test was operated with an oxygen concentration cell condition with both oxygen and water gradients on BCF dense pellet samples:

Air-3.12% H_2O , Ag electrode(I)/BCF/Ag electrode(II), O_2 -3.12% H_2O

Air-3.12% H_2O , Ag electrode(I)/BCF/Ag electrode(II), air-1.56% H_2O

To calculate the theoretical V_{cal} , it needs the partial pressures in each condition mentioned previously, assuming that the measured t_i equals 1. The transfer number t_i can be generated by dividing the measured EMFs (V_{mea}) by the calculated one (V_{cal}), as shown in the following equation:

$$t_i = \frac{V_{\text{mea}}}{V_{\text{cal}}} \quad (4)$$

For example, in an oxygen concentration cell, the partial pressure of water on each side is the same. Thus, Equation (3) transforms into the following equation:

$$V_{\text{cal}} = (t_{\text{H}^+} + t_{\text{O}_2^-}) \frac{RT}{4F} \ln \left(\frac{p_{\text{O}_2}^{\text{II}}}{p_{\text{O}_2}^{\text{I}}} \right) \quad (5)$$

Assuming $t_{\text{H}^+} + t_{\text{O}_2^-} = 1$, inserting the ideal gas constant R , the Faraday constant F , the temperature T , and partial pressures of oxygen into the equation, V_{cal} is calculated.

And for the concentration cell with a water gradient, the partial pressure of oxygen on each side is the same that Equation (3) transforms into the following equation:

$$V_{\text{cal}} = t_{\text{H}^+} \frac{RT}{2F} \ln \left(\frac{p_{\text{H}_2\text{O}}^{\text{I}}}{p_{\text{H}_2\text{O}}^{\text{II}}} \right) \quad (6)$$

Moreover, transfer numbers were corrected by considering electrode polarization with the following equation, in which R_{ele} is the electrolyte resistance, the R_{total} is the total resistance, including the R_{ele} , and the polarization resistance of electrodes.²⁹ These resistances were determined by EIS tested by Gamry Reference 3000 and fitted by equivalent circuits:

$$t_i = 1 - \frac{R_{\text{ele}}}{R_{\text{total}}} \left(1 - \frac{V_{\text{mea}}}{V_{\text{cal}}} \right) \quad (7)$$

The OCV measurement was taken by Gamry Reference 3000 at 900°C under different biases, including air/5% H_2 and air/ H_2 with a flow rate of 50 ml min⁻¹. The EIS was collected by a Gamry Reference 600 Plus at 750°C in sequenced atmospheres of wet 5% H_2 (balanced by Ar), wet air, and back to wet 5% H_2 with a flow rate of 50 ml min⁻¹ (the humidity was introduced by following through room-temperature water bubbler). The data was collected using a perturbation voltage of 10 mV and a frequency range of 0.01–5 MHz.

The obtained EIS results were analyzed by fitting output resistances to output resistances using ZView software based on the equivalent circuit model and then converting to conductivities. The resulting impedance spectra were deconvoluted with the distribution of relaxation time (DRT) program from Ciucci et al.³⁰ with regularization parameter $\lambda = 0.1$.

All cells investigated in this paper were summarized in Table 1.

3 | RESULTS AND DISCUSSION

3.1 | BCF TPOC's crystal structures

To achieve the thermodynamically stable BCF powders, we utilized the one-pot modified Pechini method to synthesize BCF powders (BCF-Multi). The atom-level dispersion of raw materials ensured the fast and complete chemical reaction at high temperatures for forming stable BCF powder. Figure 2 summarizes the XRD patterns of the BCF powders obtained at different synthesis stages. The charcoal-like primary powder (black plot in Figure 2A) obtained by drying the viscous gel at 150°C is amorphous, proving that

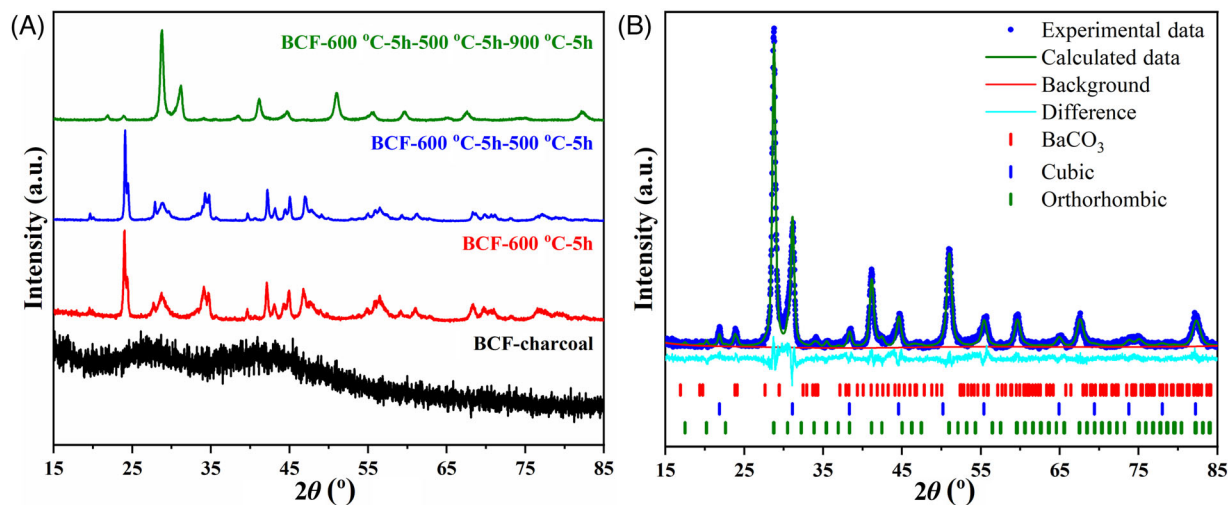


FIGURE 2 (A) X-ray diffraction (XRD) patterns of BCF powders obtained at different synthesis stages. (B) XRD Rietveld refinement result of the BCF-Multi powder

TABLE 1 Summary of cells fabricated in different configurations

No.	Cell name	Electrolyte	Electrodes
1	BCF symmetric cell on BCZYYb	BCZYYb	BCF
2	BCF symmetric cell on BZY20	BZY20	BCF
3	BCF + 20 mol% NiO symmetric cell	BCZYYb	BCF + 20 mol% NiO
4	BCF single cell	BCZYYb	BCF (cathode) BCZYYb-NiO (anode)
5	BCF-conductivity	BCF	None
6	BCF-EMF	BCF	None
7	BCF-OCV	BCF	None

Abbreviations: EMF, electromotive force; OCV, open-circuit voltage.

the metal elements in the raw materials were dispersed very well. The calcination at 600°C for 5 h in stagnant air removed the amorphous phase and formed carbonates, perovskite oxides, and simple oxides with smaller crystallite sizes (red plot in Figure 2A). The long-term ball-milling and recalcination at 500°C for 5 h in the same atmosphere (blue plot in Figure 2A) did not change the crystal structure of BCF powder compared to the one calcined at 600°C (BCF precursor powder). The further calcination at 900°C for 5 h in stagnant air (green plot in Figure 2A) formed twin perovskite phases (orthorhombic and cubic phases) with a tiny amount of barium carbonate impurity (BCF-Multi powder). The Rietveld refinement of the 900°C-calcined powder (Figure 2B) indicates that the final BCF powder comprises orthorhombic perovskite phase (73%), cubic perovskite phase (24%), and barium carbon-

ate (3%). The phase composition of the BCF composite is consistent with the literature.^{21,24,25,31} A small amount of barium carbonate was usually observed, while synthesizing barium containing perovskite oxides by calcining the charcoal-like primary powder derived from the modified Pechini method at a temperature lower than or equal to 900°C. Both the poor air exchange of the box furnace and high powder packing bed could be the reasons caused the residual barium carbonates, which can be removed by better control of the calcination process. From Figure 2, we can conclude that by calcining the charcoal-like primary powder derived from the modified Pechini method at 900°C, we can obtain the TPOCs comprising orthorhombic and cubic perovskite phases as reported in the literature.

We further studied the crystal structures of BCF powders synthesized using alternative methods and summarized the XRD patterns in Figure 3. The direct calcination of the primary charcoal powder derived from the modified Pechini method at 900°C for 5 h (BCF-Direct) resulted in TPOCs comprising orthorhombic and cubic perovskite phases without any impurity (black plot in Figure 3). The relative peak positions of the two phases of the BCF-Direct powder are consistent with the BCF-Multi shown in Figure 2A, showing that the final calcination conditions (temperature, atmosphere, and time) are the determining parameters to decide the BCF crystal structure. The pellets obtained after sintering at 1300°C for 12 h could also achieve the same phase compositions (red plot in Figure 3) as the BCF-Direct by characterizing the ground powders. It is easy to conclude that the BCF TPOCs are relatively stable in an oxidizing atmosphere (e.g., stagnant air) without noticeable phase changes with different calcination/sintering temperatures. However, the reduction-synthesized BCF powder (BCF-Reduction) by

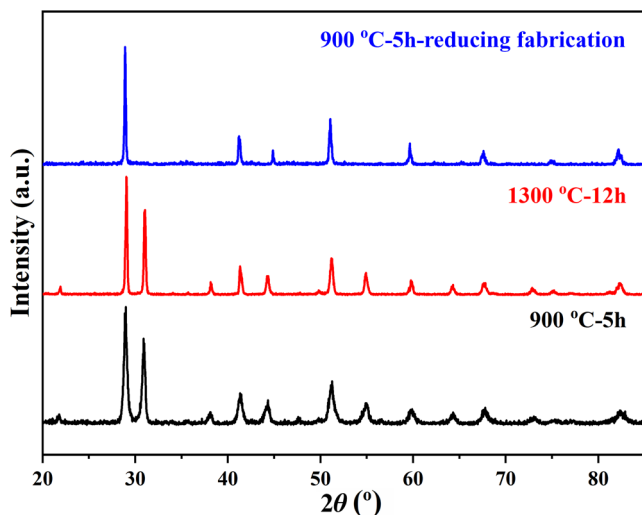


FIGURE 3 Powder X-ray diffraction (XRD) patterns of the BCF-Direct powder, BCF dense pellet sintered at 1300°C in the box furnace, and BCF powders at 900°C under 5% H₂-reduced atmospheres (BCF-Reduction)

calcining the fine BCF precursor powder at 900°C for 5 h in a reducing atmosphere (dry 5 vol% H₂ balanced by Ar) showed a pure orthorhombic perovskite crystal structure rather than TPOC (blue plot in Figure 3). No other impure peaks (e.g., iron metal) were observed in this reducing-atmosphere synthesized BCF powder, showing no precipitation. It is not surprising that the reducing atmosphere preferred the existence of lower oxidation states of Ce³⁺ and Fe²⁺/Fe³⁺ rather than Ce⁴⁺ and Fe⁴⁺, transitioning the structure to the orthorhombic perovskite, according to tolerance factors (0.939–0.847). Thus, the BCF crystal structure is susceptible to exposure atmospheres.

We further studied the temperature and atmosphere effects on the BCF crystal structure to provide more information to determine TPOC's suitability for specific applications. The BCF-Direct TPOC powder was used as an initial powder to perform treatment at different temperatures under different atmospheres. Figure 4 summarizes the XRD patterns of the BCF powders after reducing at 900, 750, and 650°C in dry 5 vol% H₂ balanced by Ar for 24 h and the ones after reoxidizing of reduced samples in the air at the same temperatures for the same time. Corresponding samples were labeled with -R for reducing atmosphere-treated ones and -RO for reoxidizing atmosphere-treated ones under air. The reduction at 900°C could fully convert the BCF TPOC to phase-pure orthorhombic perovskite oxide without any impurity or precipitation, which is consistent with the XRD patterns for the BCF powder synthesized under the same reducing atmosphere (dry 5 vol% H₂ balanced by Ar) and temperature (i.e., 900°C) as shown in Figure 3. This consistent observation indicates that the reduction for 24 h at 900°C is long enough to reach the

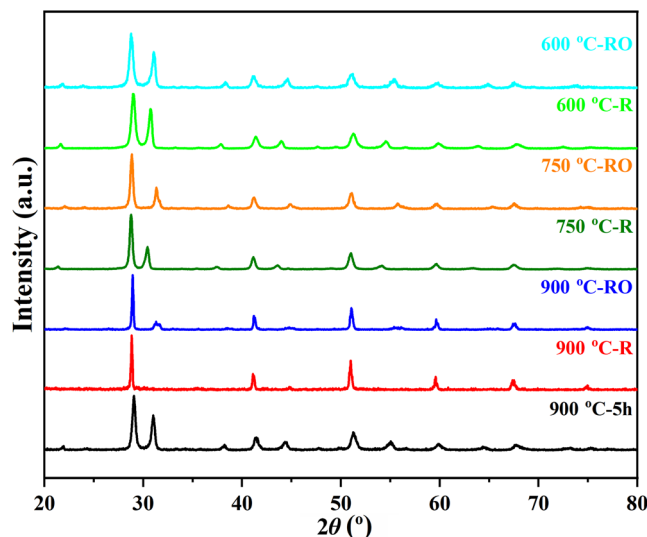


FIGURE 4 X-ray diffraction (XRD) patterns of prepared BCF-Direct (900°C 5 h), reduced samples under 5% H₂ for 24 h, and reoxidized samples of reduced ones under air for 24 h 900, 750, and 600°C, respectively

thermodynamic equilibrium. Although the reoxidation in the air at 900°C for 24 h could recover the BCF-Direct with orthorhombic and cubic perovskite phases, the percentage of the cubic phase is much lower than the original BCF TPOC before treatments (black plot in Figure 4). The enlarged particle size probably hindered this incomplete recovery of phase composition after reducing the BCF powder (Figure 5B). Compared to the redox results for the BCF powders treated at 900°C, the BCF powders reduced and reoxidized at the lower temperatures of 750 and 600°C showed very different structure evolution. The BCF-Direct TPOC powders were only partially reduced at these two temperatures. Instead of forming a phase-pure orthorhombic perovskite phase, the reduced BCF powders still comprised orthorhombic and cubic perovskite phases, although the relative density of the cubic phase decreased to some degree compared to the original BCF-Direct powder. This incomplete reduction might be caused by the intrinsic thermodynamic equilibrium or the sluggish reduction kinetics, which is under our ongoing investigation. The reoxidation at 750 and 600°C in the air for 24 h did not change the XRD patterns of the reduced BCF powders. These results indicate that reducing the original BCF TPOC powder at 750 and 600°C could prepare two new BCF TPOCs with a relatively lower percentage of cubic phase and higher orthorhombic phase, which are stable under both reducing and oxidizing atmospheres. In detail, the BCF TPOC treated at 750°C, the higher temperature, possessed a higher amount of orthorhombic phase than the one treated at 600°C, the lower temperature. Therefore, even though only 24 h of reduction and reoxidation were

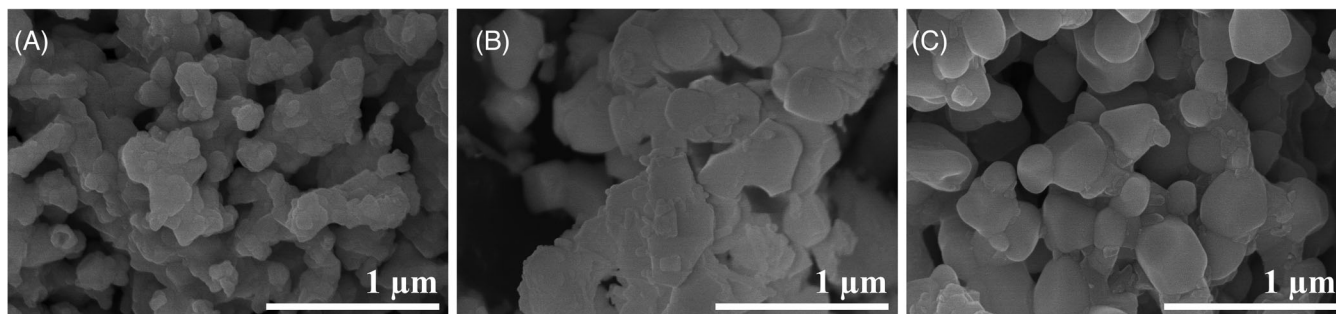


FIGURE 5 Scanning electron microscopy (SEM) images for (A) as-prepared BCF powder at 900°C, (B) reduced BCF 900-R, and (C) reoxidized BCF 900-RO powders

demonstrated, it still has the potential to obtain stable BCF TPOCs with controlled ratios between the orthorhombic and cubic perovskite phases under variable atmospheres at specific temperatures. Moreover, considering the predominant conduction properties of each perovskite phase (i.e., orthorhombic phase: proton conduction; cubic phase: mixed oxygen ion and electron conduction), different electrochemical properties could be achieved with changed phase compositions.

3.2 | Electrochemical properties under oxidizing atmospheres

The electrochemical properties were first studied by the EIS and the EMF test using dense BCF TPOC pellets. The BCF TPOC powder calcined at 900°C was dry-pressed into pellets and then sintered at 1300°C for 12 h to obtain dense BCF pellets. A dense pellet was painted with identical silver electrodes on both sides to make EIS and EMF measurements of electrochemical cells. The EIS measurement of the symmetrical cells in the wet air atmosphere was performed from 400 to 700°C. The total conductivity was calculated by the resistance (first intercept with X -axis) obtained by EIS measurement and the dimensions of the BCF dense pellet. The results (black plot in Figure 6A) show a minimal transport activation energy (i.e., 0.11 eV) at temperatures between 400 and 600°C, much lower than the activation energies for proton (around 0.4–0.6 eV) or oxygen ion (usually higher than 1.0 eV) transport. Negative temperature dependence was observed when the temperature was higher than 600°C. The less or negatively temperature-dependent conductivity usually indicates that the electronic conductivity dominates the transport behavior under this condition.²⁴

Another dense pellet with Ag current collectors was sealed on the end of an alumina tube for performing the EMF measurement to investigate the partial conduction behavior. The voltage of the concentration cell was obtained by adjusting the oxygen concentration gradient

and water concentration gradient. The wet oxidizing atmospheres were used to get the partial conduction properties, under which the BCF is relatively stable, as confirmed previously. In Figure 6B, the dependence of ionic transfer numbers on temperature indicates that the total ionic transfer number is lower than 2% in the whole temperature range (400–700°C), although a positive effect is found. The proton transfer number dominates the total ionic transport at lower temperatures, whereas the oxygen ion transfer number dominates at higher temperatures. The partial conductivities of the electron, proton, and oxygen ion were calculated using the total conductivity and the transfer numbers and displayed in Figure 6A (red, blue, and green plots). The electronic conductivity almost overlapped with the total conductivity because of the high transfer number (>98%). The oxygen ion and proton conductivities are almost two orders of magnitude lower than the electronic conductivity. The oxygen ion conductivity is higher than the proton conductivity when the temperature is higher than 550°C. It is worthy to note that, the ionic transfer numbers are too low to accurately calculate partial ionic conductivities at lower temperatures. Therefore, we can conclude that the BCF TPOC synthesized in the oxidizing atmosphere showed triple-conducting properties with predominant electronic conductivity in oxidizing atmospheres.

3.3 | Electrochemical properties under reducing/oxidizing gradients

It has been shown that the reducing atmosphere (e.g., 5 vol% H₂ balanced by Ar) can entirely reduce the TPOC powder into phase-pure orthorhombic perovskite at 900°C. As the predominant conducting properties of cubic and orthorhombic phases are different, OCVs should be built when the BCF pellets are placed under reducing (5 vol% H₂ balanced by Ar or pure H₂)/oxidizing (air) gradients, which is a crucial feature of electrolyte materials. The OCV was measured at 900°C under these

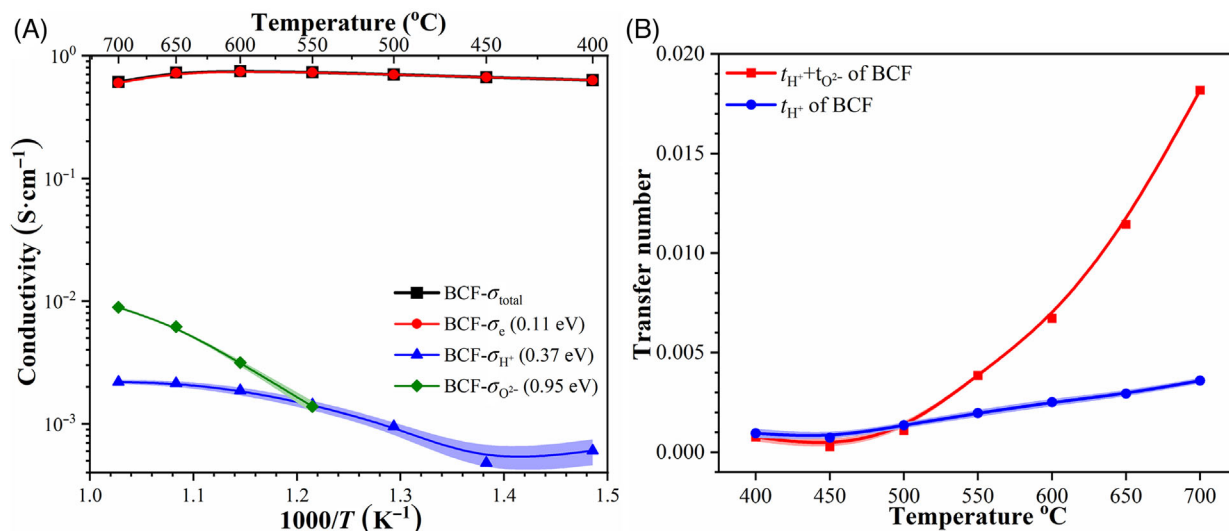


FIGURE 6 (A) Temperature dependence of total and calculated partial conductivities under wet air conditions for the BCF dense pellet. (B) Ionic transfer numbers of BCF under oxygen and water partial pressure gradients. (Error bars were labeled as the shadow areas based on standard deviations.)

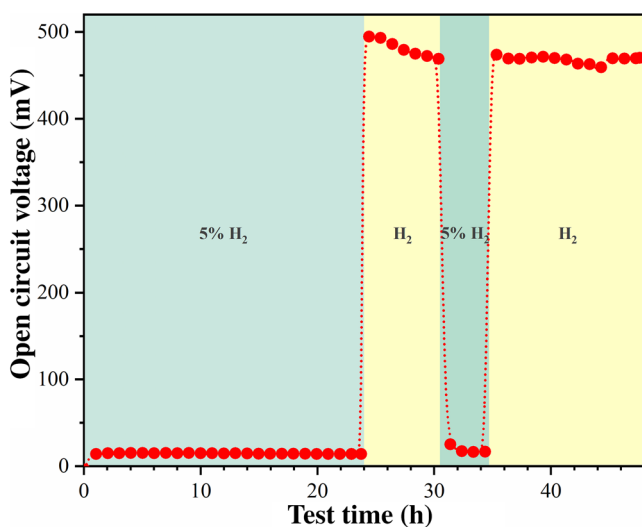


FIGURE 7 Atmosphere dependence of open-circuit voltages for the dense BCF pellet

reducing/oxidizing gradients using a dense BCF pellet with the same configuration as the EMF test. Figure 7 indicates that the OCV under air/5% H_2 gradient increased from a near-zero value to ~ 14 mV rapidly and stabilized for ~ 24 h. This experimentally measured OCV is much lower than the theoretical OCV calculated using the Nernst equation by assuming the unity of ionic transfer number, consistent with the high electron transfer number obtained by the EMF test. After using H_2 to replace 5% H_2 , the OCV jumped to ~ 500 mV and then got stable at ~ 470 mV after ~ 6 h. Once the gradient was changed back to air/5% H_2 , the potential rapidly dropped to ~ 25 mV and

kept at ~ 16 mV in the following several hours, proving that the setup was still gas tightened. When the pure H_2 was reused, the OCV fully recovered at ~ 470 mV with some fluctuation. Considering the predominated conduction in different phases discussed before, if the cubic phase was entirely reduced at 900°C like powder samples, a reduced dense pellet should offer higher OCV values than ~ 470 mV based on the Nyquist equation.

The dense BCF TPOC pellets after the OCV measurement at 900°C under the reducing/oxidizing gradient were studied to investigate the microstructure and phase composition by taking the back-scattering SEM images from different locations (reducing side, $30\ \mu\text{m}$ from the reducing side, $70\ \mu\text{m}$ from the reducing side, and oxidizing side) across the pellet cross section and comparing them with the fresh pellets sintered at 1300°C in stagnant air (Figure 8A). It is clear that the pellet still shows microstructures comprising homogeneously distributed dark grains (Fe-riched cubic phase) and bright grain (Ce-riched orthorhombic phase). It is not surprising that the microstructure at the oxidizing side (Figure 8B) looks the same as the fresh pellet (Figure 8A) as the phase composition is stable in the air atmosphere, as discussed for powder samples. However, tiny particles were observed at the grain boundary part of the surface at the reduction side (Figure 8C), indicating that the reduction reaction occurred by forming new grains at the interface between the two different types of perovskites rather than reducing the whole cubic phase grains during the reducing operation. According to the BS-SEM images, new-formed grains appear in the same color as the orthorhombic perovskite. Combined with the reduction reaction of powder

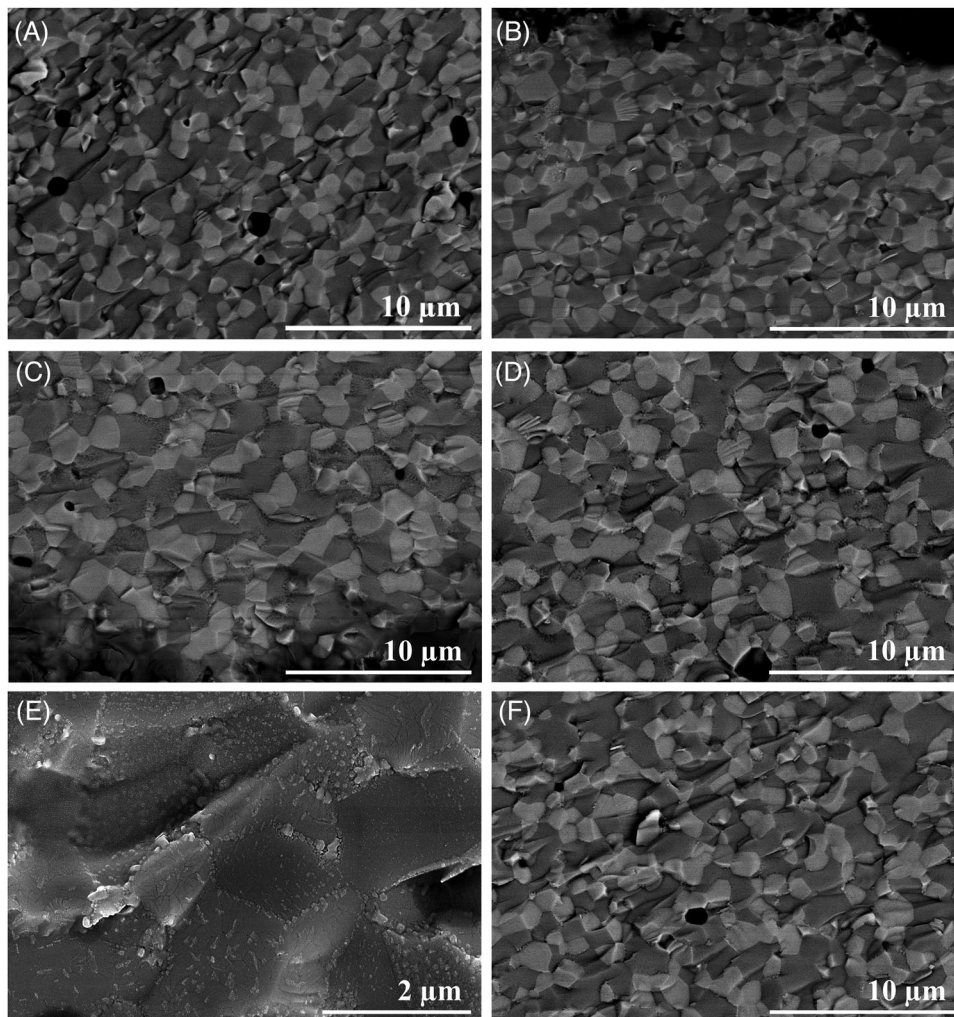


FIGURE 8 Cross-sectional back-scattering scanning electron microscopy (SEM) image for (A) the as-prepared dense BCF pellet, (B) the part contact air atmosphere, (C) the part contacts reducing atmospheres, (D) $\sim 30 \mu\text{m}$ away from the surface contact reducing atmospheres, (E) the high magnification image for the part in (D), and (F) $\sim 70 \mu\text{m}$ away from the surface contact reducing atmospheres

samples, new grains should belong to the orthorhombic phase. Small grains can also be found in the interface regions in the BS-SEM images at $\sim 30 \mu\text{m}$ (Figure 8D,E) from the reduction side. Moving the observation to $\sim 70 \mu\text{m}$ (Figure 8F) from the reduction side, we can hardly find the new-formed phases caused by reduction, indicating that the pellet established steady distribution as same as the as-prepared dense pellet of the TPOC under the oxidizing/reducing gradients. Thus, compared to powder samples, the dense pellet comprised large grains and the dense structure offered better resistance to the phase structure effects of reducing atmospheres in the microstructure aspect. The reduction reaction happened with new orthorhombic formed at the interfaces of two kinds of perovskites, responsible for the increased OCV or ionic transfer number compared to the conduction behavior in an oxidizing atmosphere. Although the OCV or the ionic transfer is not enough to allow BCF TPOC to work

as an electrolyte membrane, the sensitive OCVs changed from 25 to 470 mV when switching reducing gas from 5% H_2 to pure hydrogen directly proved the BCF's feasibility of a promising hydrogen sensor.

3.4 | Electrochemical properties under cathodic conditions of PCFCs

The excellent structural stability and triple conductivity under oxidizing atmospheres in a large temperature range (room temperature to 1300°C), demonstrated in the previous sections, make it a potential cathode material for PCFCs. The BCF electrodes were applied to BZY20 and BCZYYb electrolyte pellets to prepare symmetric cells for measuring the oxygen reduction reaction performance in the air using EIS measurement. Figure 9A,B provides the SEM images of BCF cathodes on both BZY20 and BCZYYb

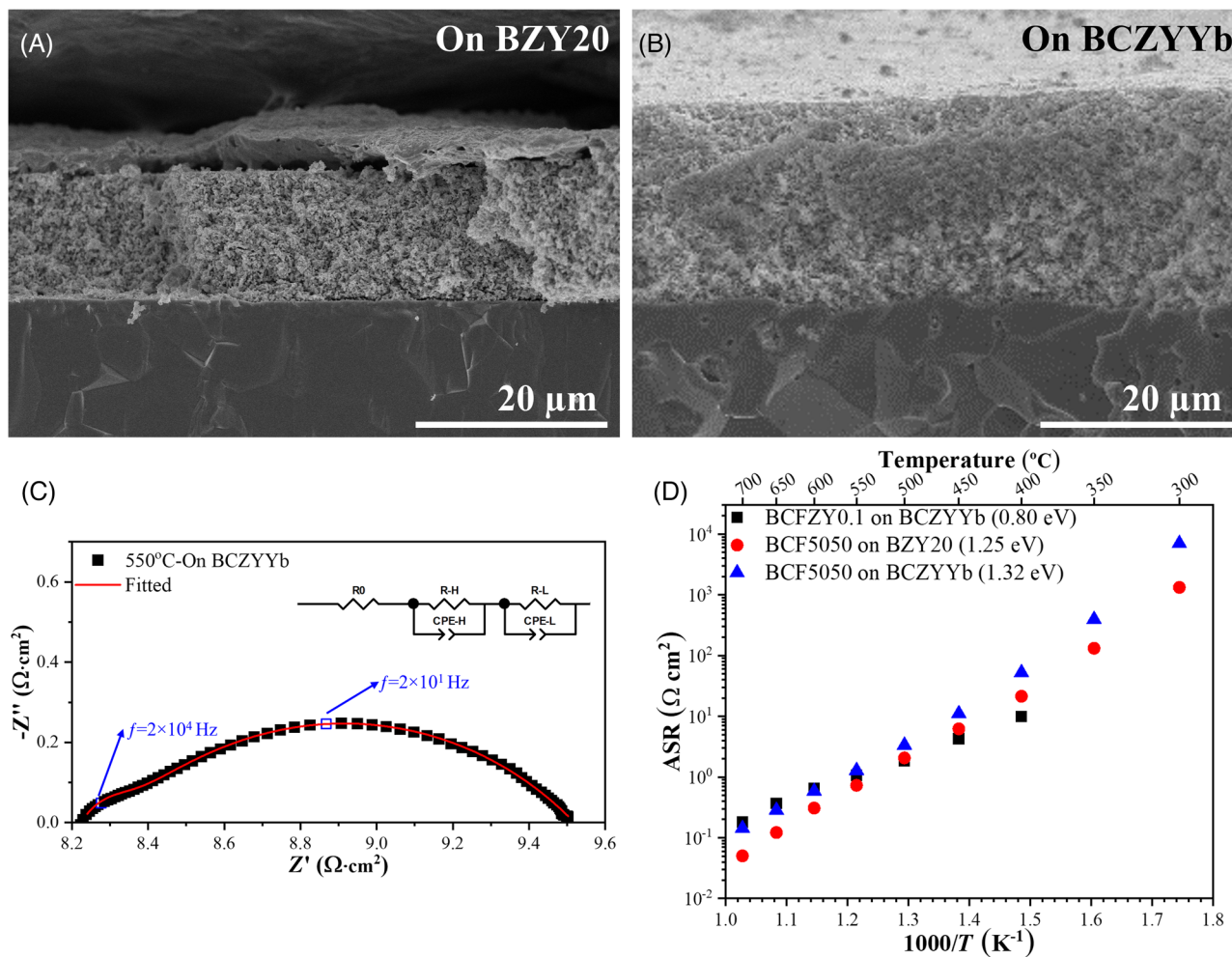


FIGURE 9 Cross-sectional scanning electron microscopy (SEM) images for the BCF electrodes on (A) BZY20 and (B) BCZYYb electrolytes, respectively. (C) The example fitting of the electrochemical impedance spectra (EIS) plot of the BCF on the BCZYYb sample was tested at 550°C (the inset is the equivalent circuit used for fitting). And (D) temperature dependence of area-specific resistance (ASR) values of BCF electrodes on different electrolytes compared with the values of state-of-the-art cathode materials BCFZY0.1 on BCZYYb electrolyte⁷

pellets, indicating that similar excellent porous nanostructures were formed on both electrolytes. An example EIS result of BCF on BCZYYb at 550°C and its fitting curve is displayed in Figure 9C, in which the Nyquist plot consists of an intercept at the X-axis at high frequency, two depressed small semicircles at both high-frequency range (R-H) and low-frequency range (R-L). The equivalent circuit model (inset in Figure 9C) was utilized to fit raw data by ZView software. Figure 9D summarizes the area-specific resistances (ASRs) of BCF cathodes on both electrolytes versus operating temperatures. The performance was also compared with the state-of-the-art triple conducting oxide cathode of BCFZY0.1. The BCF TPOC cathodes show activation energies (1.25 eV BZY20 and 1.32 eV on BCZYYb) higher than the BCFZY0.1 cathode on BCZYYb (0.80 eV). In detail, the good ASRs of 0.31 and 0.59 $\Omega \cdot \text{cm}^2$ were obtained on BZY20 and BCZYYb electrolytes at 600°C, respectively. However, the ASRs for

BCF TPOC cathodes achieved similar or better ASRs at high temperatures (550–700°C). For the ASRs at low temperatures (550–300°C), the BCF TPOC cathodes showed lower values than the BCFZY0.1 cathode. Therefore, we can conclude that BCF TPOC can work as an excellent high-temperature cathode for PCFCs.

Another cell was fabricated based on the half-cell of BCZYYb with the configuration of BCF/BCZYYb/BCZYYb + 60 wt% NiO to evaluate the performance of BCF as the cathode of PCFCs. Figure 10 summarizes the cell performance and EIS analysis for the single cells at 550–700°C under the H_2 /air gradient and the SEM image of the tested cells. The I - V and I - P curves (Figure 10A) show that the single cells' OCVs at 700, 650, 600, and 550°C, respectively, are 1.003, 1.005, 1.024, and 1.047 V, which are close to the theoretical OCV values at these temperatures, indicating the negligibly small electronic leak through electrolyte film and the excellent

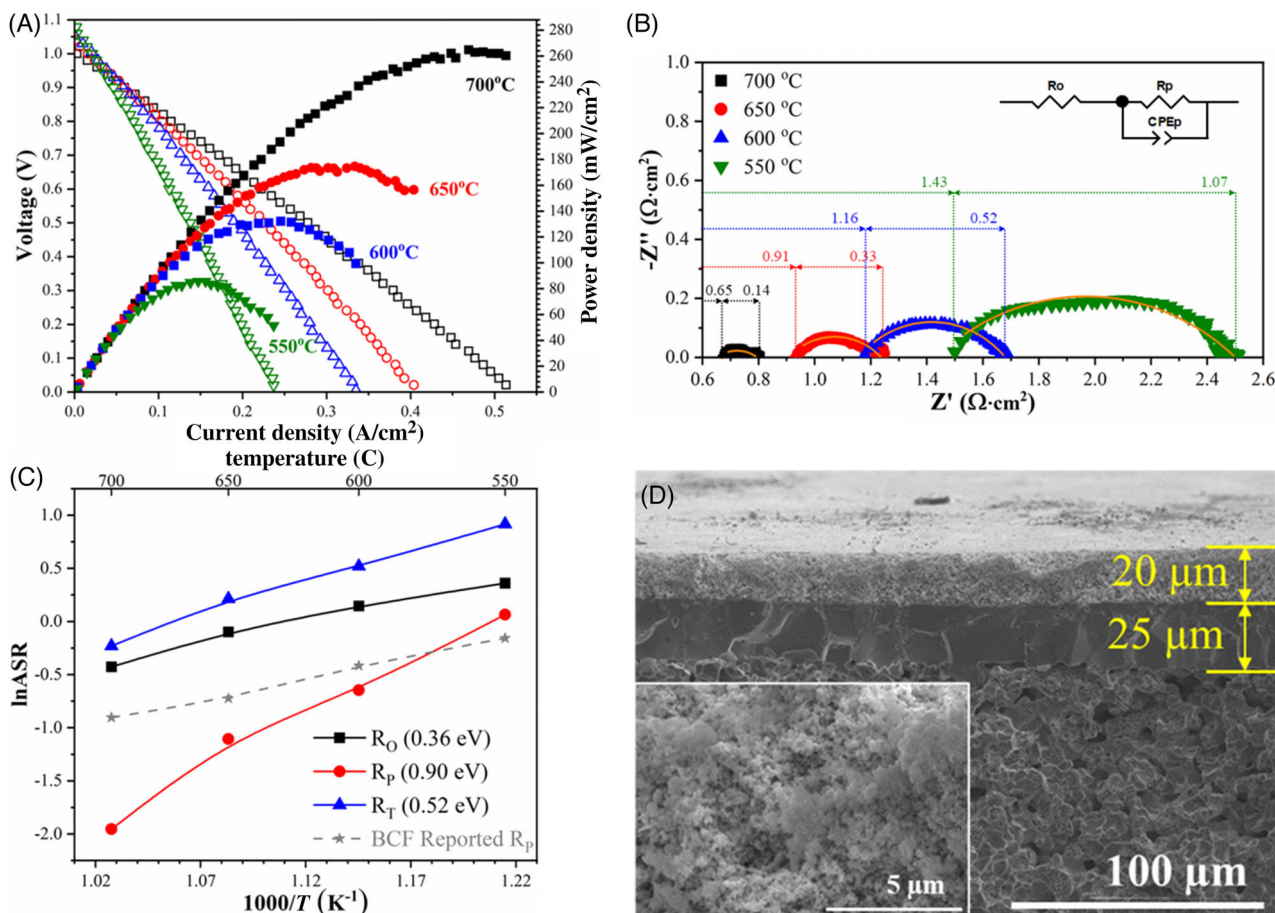


FIGURE 10 (A) Single-cell I - V and I - P curves at various temperatures in a dry hydrogen atmosphere. (B) The electrochemical impedance spectra (EIS) data for fuel cells at 550–700°C. (C) The polarization, ohmic, and total resistances are determined from the EIS. (D) The cross-sectional morphology of the single-cell after testing

gas-tight cell sealing. The peak power densities at corresponding temperatures are 265, 175, 133, and 86 mW cm². Figure 10B presents the open circuit EIS analysis results for the single cells under air/H₂ gradient at different temperatures. The experimental data markers of the Nyquist plot measured at investigated temperatures of 550–700°C have intercepts on the Z -real axis, ascribing to the ohmic resistance (R_O). The rest of the data markers at the lower frequency range respond to the polarization resistance (R_P). The fitting spectra by ZView software using the equivalent circuit model (inset in Figure 10B) allowed the determination of R_O , R_P , and the total resistance R_T . The R_O decreases from 1.43 to 0.65 Ω cm² as the temperature rises from 550 to 700°C. The calculated conductivities of the electrolyte film are 1.7, 2.2, 2.8, and 3.8 mS cm⁻¹ at 550°C, respectively, 600, 650, and 700°C, based on the electrolyte thickness of 25 μ m (Figure 10D). The values are much larger than the conductivities at corresponding temperatures for the BCZYYb pellet measured under wet 5% H₂. Therefore, there must have some extra resources for the high ohmic resistances, which need further

investigation. The polarization ASRs (R_P) at 700, 650, 600, and 550°C are 0.14, 0.33, 0.52, and 1.07 Ω cm², respectively. Compared with the reported cathode BCF (gray plot in Figure 10C), the R_P around 0.75 Ω cm² is bigger than our value (~31% improvement) at 600°C,²¹ which indicates the improvement of the performance of BCF prepared by our multistep-modified Pechini method as the cathode. Thus, the modified Pechini method derived BCF is a promising candidate as a TPOC cathode of PCFCs. Figure 10D shows the SEM image of the single-cell cross section after the performance testing. The adhesion between the cathode and the electrolyte is still excellent. The cathode and anode layers keep good porosity.

3.5 | Electrochemical properties under anodic conditions of PCFCs

The BCF TPOC was also characterized under anodic conditions to check the electrochemical properties as the dominated orthorhombic perovskite phase exhibits

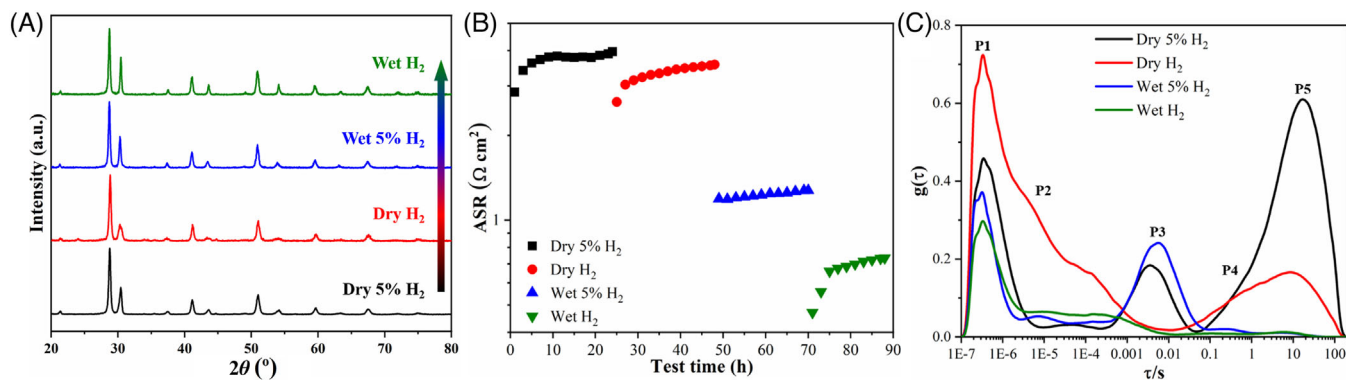
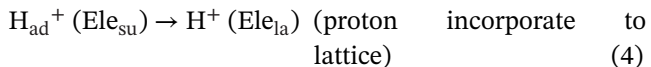
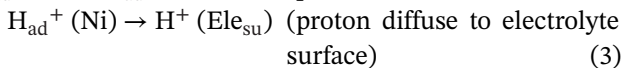
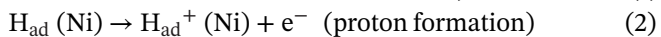
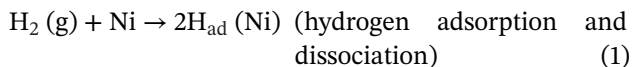


FIGURE 11 (A) X-ray diffraction (XRD) patterns of BCF powders at the end of each treatment atmosphere (24 h for every process). (B) Area-specific resistances (ASR) value versus atmosphere. (C) Distribution of relaxation time (DRT) analysis of the impedance spectra obtained at the end of each atmosphere

proton conduction in reducing atmospheres. BCF + 20 mol% NiO was utilized to characterize and analyze impedance spectra under different atmospheres combined with the DRT method at 750°C. The NiO was added to improve the electronic conductivity and the catalyst for the H₂ absorption, which is commonly used in PCFCs' anode. The phase evolution of the BCF-Direct powder was used to simulate the phase evolution during the sequenced atmosphere change (Figure 11A). For the anode part of PCFCs, possible elementary reactions are listed as following³²:



As shown in Figure 11B, with the atmosphere changing from dry 5% H₂ to dry H₂, wet 5% H₂, and then wet H₂, the ASR values show an apparent decrease indicating that the proton conduction exhibited and showed the dominance inside the sample, which greatly affected by increasing $p_{\text{H}_2\text{O}}$ and p_{H_2} . This feature fits the requirement of anode materials based on elementary reactions. Furthermore, considering the more significant amount of cubic phase (with mixed oxygen ion and electron conduction) in wet reducing atmospheres than in dry ones, the extra charge carriers under wet atmospheres also contributed to the ASR decrease.

The DRT method was applied to unravel different elementary steps that cannot be determined in the EIS as mentioned previously.^{32–35} In Figure 11C, five peaks can be observed in the curve of $g(\tau)$ versus τ (relaxation time), denoted as P1–P5, ranging from low relaxation time (LRT)

to high relaxation time (HRT). The peaks indicate the possible five processes detectable for BCF under each condition. The LRT range P1 and P2 below 10^{-4} are related to the charge transfer at the interface. The middle relaxation time (MRT) range P3 near 10^{-3} is associated with ion diffusion. The HRT range P4 and P5 above 10^{-2} represent the surface's gas diffusion and adsorption processes.³⁴ The intensity of $g(\tau)$ for P1 is reversed with the order of the relative amount of cubic perovskite phase (Figure 11A), the mixed ionic and electronic conducting phase. In the LRT range, the P1 is more prone to the electronic transfer process at the interfaces between two perovskite phases or between the perovskite phase and Ni, considering that protonic conduction dominates the conduction process under a reducing atmosphere. The P2, located in the LRT range, responds to the interface's protonic transfer. This process was promoted, with almost negligible intensity, by the extra catalytic activity of Ni, except the one under dry H₂ with the sluggish electronic transfer, which may hinder the protonic transfer. In the MRT range, the P3 shows a strong dependence of p_{H_2} , whereas the intensity of $g(\tau)$ decreases along with the increase of p_{H_2} , indicating this process represents the intragrain proton diffusion. Finally, in the HRT range, the P4 shows the dependence of $p_{\text{H}_2\text{O}}$ and exhibits the same tendency of the relative amount of cubic phase change, which hints that P4 may represent the H₂O decomposition and O²⁻ diffusion at the surface of materials, especially at the cubic phase. The P5 reveals the dependence of both $p_{\text{H}_2\text{O}}$ and p_{H_2} and takes the responsibility for H₂O absorption at the surface. Consequently, BCF + NiO exhibits the triple-conducting properties under reducing atmospheres at 750°C with repressed conductivity showing low ASR values than the typical requirement of anode materials for PCFCs. Furthermore, combined with the microstructure change after reducing atmosphere treatments on BCF powder samples and dense pellets, the XRD patterns of sequentially treated BCF powders under

reducing atmospheres at 750°C prove that the TPOC BCF shows a continuous change versus the treatment time, leading to undesired consequences in the practical anodic applications.

4 | CONCLUSIONS

This work conducted a series of experiments to carefully investigate the phase compositional, microstructural, and electrochemical change of BCF dual-phase material, consisting of cubic and orthorhombic perovskite phases, based on various atmospheres and temperatures. XRD patterns and SEM images of BCF powders after different treatments show that the cubic perovskite phase is sensitive to the reducing atmospheres, which could be reduced into an orthorhombic phase above 600°C by the reaction happened at interfaces between the two phases. Besides, microstructures show apparent change after the treatment due to the reduction reaction, which dramatically affects the reoxidation of cubic phases. Electrochemical characterizations on BCF dense pellets illustrate the coexistence of multi-ionic conductions and electronic conduction. Apparent conducting property varies based on the phase composition and microstructure changes as predominate conduction in each phase is different.

Furthermore, as per these changes, a better understanding of the electrochemical properties of BCF samples was achieved by investigating the reducing/oxidizing gradients, cathodic conditions, and anodic conditions were conducted to get insight into BCF for electrochemical cell applications. BCF shows hydrogen partial pressure change sensitivity under the reducing/oxidizing gradients, which established OCV change from ~16 to ~470 mV in a short period. Combined modified Pechini method, triple-conducting BCF achieved a more competitive performance than the state-of-the-art cathode materials BCFZY0.1 in ASR. Furthermore, demonstrated single cell achieves better performance than the previous report,²¹ showing ~31% less polarization resistance at 600°C. Last, under anodic conditions, the BCF shows multi-ionic conduction and electronic conduction, accompanied by phase composition and microstructure changes that hinder the achievability of good anodic performance. The understanding of apparent properties variation under different conditions according to the phase evolution guided the future research of BCF and showed an exemplar analysis methodology for other TPOCs.

ACKNOWLEDGMENTS

This article is based upon work supported by the US Department of Energy's Office of Energy Efficiency and Renewable Energy (EERE) under the Fuel Cell Technolo-


gies Office Award Number DE-EE0008428. This work was also supported in part by the National Aeronautics and Space Administration (NASA) under Grant no. #80NSSC20M0233 (NASA).

DISCLAIMER

“This report was prepared as an account of work sponsored by an agency of the United States Government. Neither the United States Government nor any agency thereof, nor any of their employees, makes any warranty, express or implied, or assumes any legal liability or responsibility for the accuracy, completeness, or usefulness of any information, apparatus, product, or process disclosed, or represents that its use would not infringe privately owned rights. Reference herein to any specific commercial product, process, or service by trade name, trademark, manufacturer, or otherwise does not necessarily constitute or imply its endorsement, recommendation, or favoring by the United States Government or any agency thereof. The views and opinions of authors expressed herein do not necessarily state or reflect those of the United States Government or any agency thereof.”

ORCID

Zeyu Zhao  <https://orcid.org/0000-0001-8649-925X>

Harrison Wofford  <https://orcid.org/0000-0002-3002-907X>

Jianhua Tong  <https://orcid.org/0000-0002-0684-1658>

REFERENCES

1. Gao Z, Mogni LV, Miller EC, Railsback JG, Barnett SA. A perspective on low-temperature solid oxide fuel cells. *Energy Environ Sci*. 2016;9(5):1602–44.
2. Zhang Y, Knibbe R, Sunarso J, Zhong YJ, Zhou W, Shao ZP, et al. Recent progress on advanced materials for solid-oxide fuel cells operating below 500°C. *Adv Mater*. 2017;29(48):1700132.
3. Zhou Y, Guan XF, Zhou H, Ramadoss K, Adam S, Liu HJ, et al. Strongly correlated perovskite fuel cells. *Nature*. 2016;534(7606):231–4.
4. Hossain S, Abdalla AM, Jamain SNB, Zaini JH, Azad AK. A review on proton conducting electrolytes for clean energy and intermediate temperature-solid oxide fuel cells. *Renew Sustainable Energ Rev*. 2017;79:750–64.
5. Wachsman ED, Lee KT. Lowering the temperature of solid oxide fuel cells. *Science*. 2011;334(6058):935–9.
6. Li MR, Zhou W, Zhu ZH. Recent development on perovskite-type cathode materials based on SrCoO_{3-δ} parent oxide for intermediate-temperature solid oxide fuel cells. *Asia-Pac J Chem Eng*. 2016;11(3):370–81.
7. Duan CC, Tong JH, Shang M, Nikodemski S, Sanders M, Ricote S, et al. Readily processed protonic ceramic fuel cells with high performance at low temperatures. *Science*. 2015;349(6254):1321–6.
8. Peng RR, Wu TZ, Liu W, Liu XQ, Meng GY. Cathode processes and materials for solid oxide fuel cells with proton conductors as electrolytes. *J Mater Chem*. 2010;20(30):6218–25.

9. Shang M, Tong JH, O'Hayre R. A promising cathode for intermediate temperature protonic ceramic fuel cells: $\text{BaCo}_{0.4}\text{Fe}_{0.4}\text{Zr}_{0.2}\text{O}_{3-\delta}$. *RSC Adv.* 2013;3(36):15769–75.
10. Norby T. Advances in proton ceramic fuel cells, steam electrolyzers, and dehydrogenation reactors based on materials and process optimizations. *ECS Trans.* 2017;80(9):23.
11. Zhou C, Sunarso J, Song YF, Dai J, Zhang JX, Gu BB, et al. New reduced-temperature ceramic fuel cells with dual-ion conducting electrolyte and triple-conducting double perovskite cathode. *J Mater Chem A.* 2019;7(21):13265–74.
12. Fan LD, Su PC. Layer-structured $\text{LiNi}_{0.8}\text{Co}_{0.2}\text{O}_2$: a new triple ($\text{H}^+/\text{O}^{2-}/\text{e}^-$) conducting cathode for low temperature proton conducting solid oxide fuel cells. *J Power Sources.* 2016;306:369–77.
13. Kim J, Sengodan S, Kwon G, Ding D, Shin J, Liu ML, et al. Triple-conducting layered perovskites as cathode materials for proton-conducting solid oxide fuel cells. *ChemSusChem.* 2014;7(10):2811–5.
14. Papac M, Stevanovi V, Zakutayev A, O'Hayre R. Triple ionic-electronic conducting oxides for next-generation electrochemical devices. *Nat Mater.* 2021;20(3):301–13.
15. Zhu AK, Zhang GL, Wan T, Shi TT, Wang H, Wu MZ, et al. Evaluation of $\text{SrSc}_{0.175}\text{Nb}_{0.025}\text{Co}_{0.8}\text{O}_{3-\delta}$ perovskite as a cathode for proton-conducting solid oxide fuel cells: the possibility of in situ creating protonic conductivity and electrochemical performance. *Electrochim Acta.* 2018;259:559–65.
16. Matsui T, Manriki K, Miyazaki K, Muroyama H, Eguchi K. A new oxygen reduction electrocatalyst of barium lanthanide cobaltate for composite cathodes of proton-conducting ceramic fuel cells. *J Mater Chem A.* 2018;6(29):14188–94.
17. Zhang ZB, Wang J, Chen YB, Tan SZ, Shao ZP, Chen DJ. In situ formation of a 3D core-shell and triple-conducting oxygen reduction reaction electrode for proton-conducting SOFCs. *J Power Sources.* 2018;385:76–83.
18. Shah M, Voorhees PW, Barnett SA. Time-dependent performance changes in LSCF-infiltrated SOFC cathodes: the role of nano-particle coarsening. *Solid State Ionics.* 2011;187(1):64–7.
19. Lin Y, Fang SM, Su D, Brinkman KS, Chen FL. Enhancing grain boundary ionic conductivity in mixed ionic-electronic conductors. *Nat Commun.* 2015;6:6824.
20. Wu YS, Hou J, Gong Z, Miao LN, Tang HD, Liu W. High performance $\text{BaCe}_{0.5}\text{Fe}_{0.5-x}\text{Bi}_x\text{O}_{3-\delta}$ as cobalt-free cathode for proton-conducting solid oxide fuel cells. *J Alloys Compd.* 2019;790:551–7.
21. Tao ZT, Bi L, Zhu ZW, Liu W. Novel cobalt-free cathode materials $\text{BaCe}_x\text{Fe}_{1-x}\text{O}_{3-\delta}$ for proton-conducting solid oxide fuel cells. *J Power Sources.* 2009;194(2):801–4.
22. Song Y, Chen Y, Wang W, Zhou C, Zhong Y, Yang G, et al. Self-assembled triple-conducting nanocomposite as a superior protonic ceramic fuel cell cathode. *Joule.* 2019;3(11):2842–53.
23. Zhao ZY, Cui J, Zou MD, Mu SL, Huang H, Meng YQ, et al. Novel twin-perovskite nanocomposite of Ba-Ce-Fe-Co-O as a promising triple conducting cathode material for protonic ceramic fuel cells. *J Power Sources.* 2020;450:227609.
24. Zhu L, Hong T, Xu CX, Cheng JG. A novel dual phase $\text{BaCe}_{0.5}\text{Fe}_{0.5}\text{O}_{3-\delta}$ cathode with high oxygen electrocatalysis activity for intermediate temperature solid oxide fuel cells. *Int J Hydrogen Energy.* 2019;44(29):15400–8.
25. Cheng SF, Wang YJ, Zhuang LB, Xue J, Wei YY, Feldhoff A, et al. A dual-phase ceramic membrane with extremely high H_2 permeation flux prepared by autoseparation of a ceramic precursor. *Angew Chem Int Ed.* 2016;55(36):10895–8.
26. Zhu XF, Wang HH, Yang WS. Novel cobalt-free oxygen permeable membrane. *Chem Commun.* 2004;10(9):1130–1.
27. Qi H, Zhang T, Cheng M, Liu D, Tu B. Rational design of the self-assembled $\text{BaCo}_{1-x}\text{Zr}_x\text{O}_{3-\delta}$ ($x = 0.8-0.2$) nanocomposites as the promising low/intermediate-temperature solid oxide fuel cell cathodes. *J Eur Ceram Soc.* 2021;42:1042–52.
28. Han DL, Noda Y, Onishi T, Hatada N, Majima M, Uda T. Transport properties of acceptor-doped barium zirconate by electromotive force measurements. *Int J Hydrogen Energy.* 2016;41(33):14897–908.
29. Liu ML, Hu HX. Effect of interfacial resistance on determination of transport properties of mixed-conducting electrolytes. *J Electrochem Soc.* 1996;143(6):L109–12.
30. Wan TH, Saccoccio M, Chen C, Ciucci F. Influence of the discretization methods on the distribution of relaxation times deconvolution: implementing radial basis functions with DRT-tools. *Electrochim Acta.* 2015;184:483–99.
31. Hu T, Liang W, Xia X, Peng H, Jiang H. Simultaneous production of pure nitrogen and syngas in $\text{BaCe}_{0.5}\text{Fe}_{0.5}\text{O}_{3-\delta}$ membrane reactor. *Catal Today.* 2021;364:125–31.
32. Shi N, Su F, Huan DM, Xie Y, Lin J, Tan WZ, et al. Performance and DRT analysis of P-SOFCs fabricated using new phase inversion combined tape casting technology. *J Mater Chem A.* 2017;5(37):19664–71.
33. Tian HC, Li WY, Ma L, Yang T, Guan B, Shi WY, et al. Deconvolution of water-splitting on the triple-conducting Ruddlesden-Popper-phase anode for protonic ceramic electrolysis cells. *ACS Appl Mater Interfaces.* 2020;12(44):49574–85.
34. Danilov N, Tarutin A, Lyagaeva J, Vdovin G, Medvedev D. CO_2 -promoted hydrogen production in a protonic ceramic electrolysis cell. *J Mater Chem A.* 2018;6(34):16341–6.
35. Zhang YX, Chen Y, Yan MF, Chen FL. Reconstruction of relaxation time distribution from linear electrochemical impedance spectroscopy. *J Power Sources.* 2015;283:464–77.

How to cite this article: Zhao Z, Zou M, Huang H, Zhai X, Wofford H, Tong J. Insight of $\text{BaCe}_{0.5}\text{Fe}_{0.5}\text{O}_{3-\delta}$ twin perovskite oxide composite for solid oxide electrochemical cells. *J Am Ceram Soc.* 2023;106:186–200.
<https://doi.org/10.1111/jace.18643>